Integrating Materials and Manufacturing Innovation
https://doi.org/10.1007/s40192-021-00208-5

THEMATIC SECTION: METAL ADDITIVE MANUFACTURING MODELING CHALLENGE SERIES 2020

Microscale Structure to Property Prediction for Additively Manufactured IN625 through Advanced Material Model Parameter Identification

Sourav Saha[1] · Orion L. Kafka[2] · Ye Lu[3] · Cheng Yu[3] · Wing Kam Liu[3]

Received: 6 March 2021 / Accepted: 8 April 2021

Abstract

Challenge 4 of the Air Force Research Laboratory additive manufacturing modeling challenge series asks the participants to predict the grain-average elastic strain tensors of a few specific *challenge grains* during tensile loading, based on experimental data and extensive characterization of an IN625 test specimen. In this article, we present our strategy and computational methods for tackling this problem. During the competition stage, a characterized microstructural image from the experiment was directly used to predict the mechanical responses of certain challenge grains with a genetic algorithm-based material model identification method. Later, in the post-competition stage, a proper generalized decomposition (PGD)-based reduced order method is introduced for improved material model calibration. This data-driven reduced order method is efficient and can be used to identify complex material model parameters in the broad field of mechanics and materials science. The results in terms of absolute error have been reported for the original prediction and re-calibrated material model. The predictions show that the overall method is capable of handling large-scale computational problems for local response identification. The re-calibrated results and speed-up show promise for using PGD for material model calibration.

Keywords Additive manufacturing · IN625 · Elastic strain · Data-driven method · Proper generalized decomposition

Introduction

Metal additive manufacturing (AM) has been the focus of researchers and engineers as a promising manufacturing method for large-scale, customized, and complex metallic parts [1–3]. However, major concerns in the field of metal additive manufacturing are microstructural heterogeneity and residual strain resulting from the high spatial thermal gradients, localized heating and cooling, and fast cooling rates present in AM builds [4, 5]. The resulting microstructure of the build controls the mechanical properties [6–8]. Therefore, accurate computational models that can predict the microstructure-level evolution of strain during service conditions are crucial to enable confident engineering with these materials without an extensive retesting procedure after any part of the manufacturing process is altered [9]. Challenge 4 of the Air Force Research Laboratory (AFRL) additive manufacturing (AM) modeling challenge series centers on developing and validating reliable computational models that can track the evolution of grain-average elastic strain of certain grains under uniaxial loading conditions. In this paper, a fast Fourier transformation (FFT)-based method has been used to model the evolution of strain, both elastic and plastic, with a crystal plasticity material model. Optimization of the material model is performed by a proper

✉ Ye Lu
ye.lu@northwestern.edu

✉ Wing Kam Liu
w-liu@northwestern.edu

Sourav Saha
SouravSaha2023@u.northwestern.edu

[1] Theoretical and Applied Mechanics, Northwestern University, Evanston, IL, USA

[2] Materials Measurement Laboratory, Applied Chemicals and Materials Division, National Institute of Standards and Technology (NIST), Boulder, CO, USA

[3] Department of Mechanical Engineering, Northwestern University, Evanston, IL, USA

generalized decomposition (PGD) method [10, 11] and the performance is compared with the genetic algorithm [12].

Validating the prediction of mechanical response of material at the micro-level was the goal of the challenge and was achieved using high-energy diffraction microscopy techniques [13–15], where multiple levels of detail can be captured by combining near- and far-field imaging. The details of the high-energy diffraction methodology followed to characterize the challenge material, the nickel-based superalloy IN625, are discussed in on the Challenge Website [16], and in an article under the same Topical Collection as this paper. Necessary information on the experiments to understand the work presented here are discussed in the "Problem Statement" section.

For microscale continuum modeling of metal polycrystals, computational crystal plasticity is a common method [17–19]. While the mathematical algorithm used to solve the problem remains similar, depending on the physics to be modelled, different variations of the crystal plasticity material model have been proposed. The material models are used within, e.g., the finite element method (FEM) or the fast Fourier transformation (FFT) method [20–22] for computing the materials response. One major drawback of using crystal plasticity is the computation becomes more expensive than when more simple material models are used. Using FFT instead of FEM can improve computational efficiency, but FFT requires a periodic simulation domain, which is not always possible, or necessitates modeling compromises. Recently, data-driven mechanistic approaches have been proposed such as self-consistent clustering analysis (SCA) [23, 24] where material points are grouped together to predict the overall response of the material domain. Considering the nature of the domain given and the nature of the challenge, the group opted to use the crystal plasticity-FFT as the solution method.

Irrespective of the scenario, crystal plasticity material models involve a number of parameters to be calibrated against the experimental data before they can be used. This involves an optimization process in which material model parameters are varied and the resulting predictions compared against experimental, or otherwise ground truth, data. This optimization method requires solving for the mechanical response using crystal plasticity multiple times. As a result, the calibration can be computationally expensive, and an alternate way to calibrate the material model is desirable. One typical method for calibration is the multi-objective genetic algorithm [21, 25]. The material model used when reporting challenge results was calibrated using such a method. The results from the competition indicated that material model calibration was a key area for advancement. Thus, an advanced PGD-based optimization was applied to the material model calibration, and in this manuscript we demonstrate its high efficiency for this problem. PGD is a projection-based model reduction method and has gained popularity in recent years. This kind of approach is used for accelerated numerical simulations [26–29] or efficient parametric studies [30–33]. PGD approaches can be implemented in either intrusive or non-intrusive ways. The non-intrusive kind can be mainly based on data and therefore applicable for a wide range of problems. The method we present in this work is non-intrusive and data-driven and can be adopted for many other problems, such as for different linear and nonlinear processes or materials optimization.

The article is organized as follows: In the "Problem Statement" section describes the problem statement for the challenge and in the "Material Modeling Methods" section illustrates the solution methodology we followed. In the "Genetic Algorithm" section describes the initial genetic algorithm (GA)-based material calibration, while in the "Proper Generalized Decomposition-Based Material Parameter Identification" section discusses the fundamentals and results of a more advanced PGD-based material parameter identification method. The results reported to the challenge (with the GA calibration) and updated analysis with PGD-based calibration are presented in the "Discussion of Results". Finally, the analysis is concluded in the "Conclusions" section.

Problem Statement

The AFRL challenge statement provided certain build, material, and loading information and asked for prediction of "grain-averaged elastic strain tensors for specified grains at specified macroscopic loading points under uniaxial tension." The goal of the challenge thus being to assess the ability of grain-scale modeling to accurately reproduce measured elastic strains within a real, relatively complex, polycrystalline setting. The following sections will provide a brief summary of the information provided and requested, along with some discussion.

Measurements of the initial and calibration data, as well as the requested prediction data at each load level, were taken using in situ testing with the Air Force/PulseRay RAMS3 load frame at the Advanced Photon Source, Argonne National Laboratory [34]. The measurements include x-ray integrated micro-computed tomography (μCT) using direct beam projections, near-field HEDM/3D x-ray diffraction (3DXRD) to quantify 3D grain structure and sub-grain orientation, and far-field HEDM/3DXRD to measure grain-resolved elastic strain tensors. A box-shaped beam was used with vertical resolution of 28.5μm to measure 19 slices at the center of the test specimen, from which the data for the challenge grains was extracted. After the test, the specimen was destructively serial sectioned using the LEROY system at the AFRL [35] to collect electron backscatter diffraction (EBSD), backscatter electron (BSE), and

Journal : Large 40192 | Article No : 208 | Pages : 15 | MS Code : 208 | Dispatch : 4-5-2021

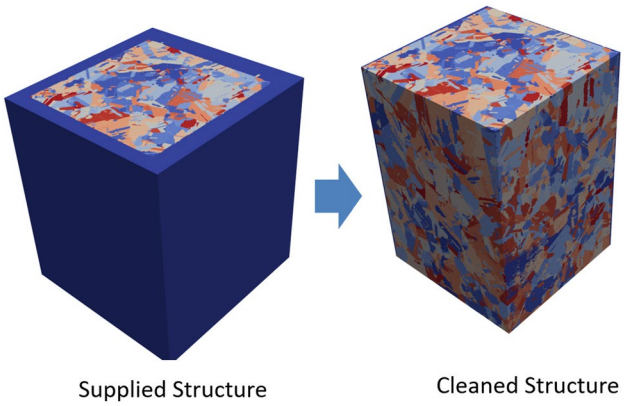

Fig. 1 Comparative diagram showing the supplied input structure after imaging and final structure used for prediction

optical microscopy (OM) images. Serial sectioning was collected with approximately 1 μm slice thickness, and similar resolution for the in-plane step size. Gold fiducial markers and μCT data were used to aid in data registration between EBSD and HEDM. Further details of all aspects of the challenge experiments, including schematics and images of the test setups, are provided on the challenge website [16] and in the manuscript by the AFRL about these experiments in this Topical Collection.

Data Provided

The AFRL provides a thorough description of the data available and methods used to collect said data on the challenge website, [16], and the article in this Topical Collection covering the experiments by the AFRL. The following items summarize the key elements needed for our models.

Material

The material is stress relieved (SR), hot isostatically pressed (HIP'ed), and heat treated (HT) AM IN625 manufactured using a commercial EOS M280[1] Laser Powder Bed Fusion (LPBF) system from gas atomized powder. Details of these post processing steps were withheld from participants. The test artifact was built with the tensile direction along the build direction and post-machined with wire electrical discharge machining, with no further finishing steps.

[1] Certain commercial software, equipment, instruments, or materials are identified in this paper to adequately specify the experimental procedure. Such identification is not intended to imply recommendation or endorsement by the National Institute of Standards and Technology, nor is it intended to imply that the equipment or materials identified are necessarily the best available for the purpose.

Characterization

Three main interconnected data streams were provided to the challenge participants. First, mechanical test information in the form of quasi-static (strain rate 10^{-4} s^{-1}) stress–strain plots both for the challenge artifact itself and for calibration was provided. The in situ challenge artifact had a unique geometric design to enable the measurements, where the calibration specimen had a more standard geometry, following the ASTM E8 standard. HEDM data (importantly, residual elastic strain) were provided at the initial state (before loading) for the challenge grains. Finally, serial sectioning electron backscatter diffraction data, collected after the specimen, were mechanically tested to collect HEDM data under various loading conditions, were registered to the HEDM dataset to define the geometry and orientation of each grain within the test specimen. Finally, a three-dimensional voxelized image of the microstructure was provided to the participants, summarizing the combined HEDM and EBSD data. The supplied input structure had different phases including IN625, pores inside the material, gold, platinum, and outer borders. A sample of the input microstructure image is shown in Fig. 1. The image was 305 voxels × 351 voxels × 312 voxels voxels, where each voxel had an edge length of 2 μm. There were 29662 features in total, including each grain, the precipitates, pore, gold, platinum, etc. Before analysis, the image was simplified to only include the IN625 grains and porosity. The porosity was modeled to be linear elastic material with extremely low stiffness. After this processing, the remaining empty air space (blue boundary region in Fig. 1a) was removed. There were in total 28 *challenge grains* specified inside the domain. These grains had a known, fixed value of initial elastic strain state at state S0 (see Fig. 2). However, there was no strain specified for any of the other grains or phases at S0.

Requested Predictions

Challenge participants were informed that HEDM measurements of grain-averaged elastic strain tensors were taken at seven different load states identified in the stress–strain curve in Fig. 2:

1. Initial, unloaded, state,
2. 100 MPa,
3. 200 MPa,
4. loaded to 300 MPa followed by a 50 MPa unload (to reduce the likelihood of creep during measurements) before measurement,
5. deformed until 0.35% strain (which was roughly 360 MPa) followed by 50 MPa unloading before measurement,

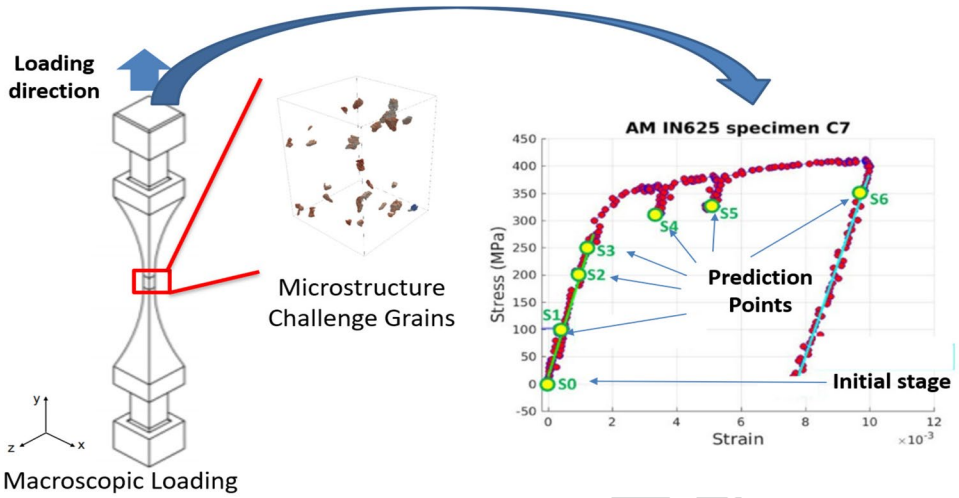

Fig. 2 Schematic diagram showing the challenge problem. The uniaxial tensile test experiment is performed, and a small section is observed under high-energy X-ray diffraction. 28 challenge grains are specified in a dataset cross-registered with electron backscatter diffraction. The initial strain of these grains is provided. The elastic strain tensors are to be predicted for these grains at specified points on the stress–strain curve (S1, S2, S3, S4, S5, S6) during the uniaxial tensile test

6. deformed until 0.5% strain (roughly 385 MPa) and unload by 50 MPa before measurement,
7. deformed until 1.0% strain (roughly 410 MPa) and unload by 50 MPa before measurement.

Participants were asked to report the grain-averaged elastic strain tensors for each of the challenge grains at each of these load states. Note that the quantity used to specific the state at which measurements and predictions were compared switches from load to strain at point four. Load control was used during the two to three hours during which measurements were taken at each load/strain level.

Some interpretation and judicious assumptions based on the data provided were required:

- The hold periods during mechanical testing of the challenge artifact were not quantified—challenge participants were told only that these periods lasted between 2 h and 3 h, and were held in load control, after a 50 MPa load reduction for holds at 300 MPa and higher. Thus, a "best guess" of the time–displacement curve to be applied as boundary values was required.
- Only the initial strain in the challenge grains, not all grains, was provided. Thus, we assumed that all other grains had zero initial strain; other approximation are possible. This approximation is the simplest possible; given the lack of data, we opted to avoid other unsubstantiated assumptions. However, the method followed in the article is general and any value of initial strain can be applied to get the solution.
- The grain structure provided was for the final state, and the assumption was that the geometry and crystallography of the initial grain structure was the same. This is an approximation, because some plastic strain (about 7.8% overall engineering strain was not recovered upon unloading) was induced.
- The single-crystal properties provided were from the literature and did not necessarily match precisely the material conditions of the test artifact. While calibration data was provided, it was on macroscale properties, rather than individual grain properties. Thus, grain-scale methods require material calibration for both physical and empirical model parameters, as we will discuss further in the following sections.
- The properties of some phases (e.g., gold and platinum fiducial markers, precipitates) were not given, although the materials appear on/in the specimen. We assumed these phases had no impact upon the mechanical response and omitted them from our analysis. However, porosity was considered in our analysis.
- Using grain-averaged properties, such as orientation and measured strains, introduces some uncertainties, as there are likely variances within the grain. However, we assumed these variations are small, thus were possible to neglect.

These challenges are mostly related to unavoidable measurement realities or are otherwise insolvable. However, identifying inherited assumptions and sources of uncertainty will help us construct a model robust to such uncertainties, and may provide insight into the differences between model and experimental results.

Calibration Data

In order to calibrate the material model, the AFRL provided us with experimental microstructure characterization and mechanical testing data [16]. For calibration, the AFRL

Journal : Large 40192 | Article No : 208 | Pages : 15 | MS Code : 208 | Dispatch : 4-5-2021

experiments used a tensile bar prepared using ASTM E8 as guidance [36]. Three post-processing steps were applied: stress relief, hot isostatic pressing, and heat treatment (SR+HIP+HT); details were not provided, and although not explicitly stated since both calibration and test specimens were described as SR+HIP+HT, we assume the post-processing for both was identical. The build direction was aligned with the tensile direction, and testing was conducted in a room temperature (75° F (23.9° C)) and laboratory air environment. The microstructure characterization information provided for the calibration specimen includes EBSD scans and back-scattered electron images from the side and top faces, and chemical analysis of powder. For this work, we only used the mechanical testing and EBSD characterization data.

Material Modeling Methods

The material model used in this work is specified in detail in [19]. For this problem, we have an initial grain average elastic strain specified. The following description is thus defined in terms of the initial deformation gradient present in the simulation.

The work uses a general elasto-viscoplastic material model. If the local deformation gradient is $\mathbf{F}$, it can be multiplicatively decomposed into individual contributions,

$$\boldsymbol{F} = \boldsymbol{F}^{e} \cdot \boldsymbol{F}^{\text{in}} \cdot \boldsymbol{F}^{\text{init}} \tag{1}$$

Here, $\mathbf{F}^e$ is elastic part of the deformation gradient, $\mathbf{F}^{\text{in}}$ is the inelastic part of the deformation gradient, and $\mathbf{F}^{\text{init}}$ is the initial part of the deformation gradient, i.e., residual deformations derived from measured elastic strains in the challenge grains.

Before applying the material model, we need to find the deformation gradient responsible for mechanical deformation $\mathbf{F}^{\text{mech}}$ by,

$$\boldsymbol{F}^{\text{mech}} = \boldsymbol{F}^{e} \cdot \boldsymbol{F}^{\text{in}} = \boldsymbol{F} \cdot \boldsymbol{F}^{\text{init}^{-1}} \tag{2}$$

The deformation gradient can be related to the elastic material model using

$$\boldsymbol{S}^{e} = \boldsymbol{C}^{\text{SE}} : \boldsymbol{E}^{e} = \frac{1}{2}\boldsymbol{C}^{\text{SE}} : \left[(\boldsymbol{F}^{e})^{T} \cdot \boldsymbol{F}^{e} - \boldsymbol{I}_{2}\right], \tag{3}$$

where $\mathbf{E}^e$ is the elastic Green–Lagrange strain, $\mathbf{S}^e$ is the second Piola–Kirchhoff stress, $\mathbf{C}^{\text{SE}}$ is the fourth-order elastic stiffness tensor, and $\mathbf{I}_2$ is the second-order identity tensor. In this work, the entire inelastic part is assumed to come from plastic deformation, i.e., $\mathbf{F}^{\text{in}} = \mathbf{F}^{p}$. The inelastic deformation gradient can be calculated from the plastic part of the material model to relate the plastic velocity gradient, $\mathbf{L}^p = \dot{\mathbf{F}}^p \cdot (\mathbf{F}^p)^{-1}$ to plastic shear rate $\dot{\gamma}^{\alpha}$ in slip system α by,

$$\boldsymbol{L}^{(p)} = \sum_{\alpha=1}^{N_{\text{slip}}} \dot{\gamma}^{(\alpha)} \left(\boldsymbol{s}_0^{(\alpha)} \otimes \boldsymbol{n}_0^{(\alpha)} \right). \tag{4}$$

Here, $\boldsymbol{s}_0^{(\alpha)}$ and $\boldsymbol{n}_0^{(\alpha)}$ are the unit vectors which define the slip direction and slip plane normal for slip system α in the undeformed configuration, N_{slip} is the number of active slip systems (active slip systems for FCC system are shown in Table 3), and $\otimes$ is the dyadic product. The resolved shear stress, $\tau^{(\alpha)}$ on the slip plane, is related to plastic shear rate $\dot{\gamma}^{(\alpha)}$. The resolved shear stress is given by,

$$\tau^{(\alpha)} = \boldsymbol{\sigma} : \left(\boldsymbol{s}^{(\alpha)} \otimes \boldsymbol{n}^{(\alpha)} \right) \tag{5}$$

where the $\boldsymbol{\sigma}$ is the Cauchy stress, $\boldsymbol{s}$ is the slip direction, and $\boldsymbol{n}$ is the slip normal, defined by:

$$\boldsymbol{\sigma} = \frac{1}{J_e}\left[\boldsymbol{F}^{e} \cdot \boldsymbol{S}^{e} \cdot (\boldsymbol{F}^{e})^{T}\right] \tag{6}$$

$$\boldsymbol{s}^{(\alpha)} = \boldsymbol{F}^{e} \cdot \boldsymbol{s}_0^{(\alpha)} \tag{7}$$

$$\boldsymbol{n}^{(\alpha)} = \boldsymbol{n}_0^{(\alpha)} \cdot (\boldsymbol{F}^{e})^{-1} \tag{8}$$

In these equations, J_e is the determinant of $\boldsymbol{F}^e$. In this work, the hardening term $\dot{\gamma}^{(\alpha)}$ evolves based on a power law, given by

$$\dot{\gamma}^{(\alpha)} = \dot{\gamma}_0 \left| \frac{\tau^{(\alpha)} - a^{(\alpha)}}{\tau_0^{(\alpha)}} \right|^{(m-1)} \left(\frac{\tau^{(\alpha)} - a^{(\alpha)}}{\tau_0^{(\alpha)}} \right), \tag{9}$$

where $\dot{\gamma}_0$ is a reference shear rate and m is the exponent related to material strain rate sensitivity. The deformation resistance shear stress τ_0 and back stress $a^{(\alpha)}$ are expressed as

$$\dot{\tau}_0^{(\alpha)} = H \sum_{\beta=1}^{N_{\text{slip}}} \left| \dot{\gamma}_0^{(\beta)} \right| - R\tau_0^{(\alpha)} \sum_{\beta=1}^{N_{\text{slip}}} \left| \dot{\gamma}_0^{(\beta)} \right|, \tag{10}$$

$$\dot{a}^{(\alpha)} = h\dot{\gamma}_0^{(\alpha)} - ra\left| \dot{\gamma}_0^{(\alpha)} \right|, \tag{11}$$

where β is a slip system, H and h are direct hardening coefficients, R and r are the dynamic recovery constants; latent and cross-hardening contributions were assumed to be identical. The FFT algorithm followed in this work is based on [37] and [38]. The implementation is fully parallel using the FFTW library [39] and can handle a simulation domain as large as provided in the challenge.

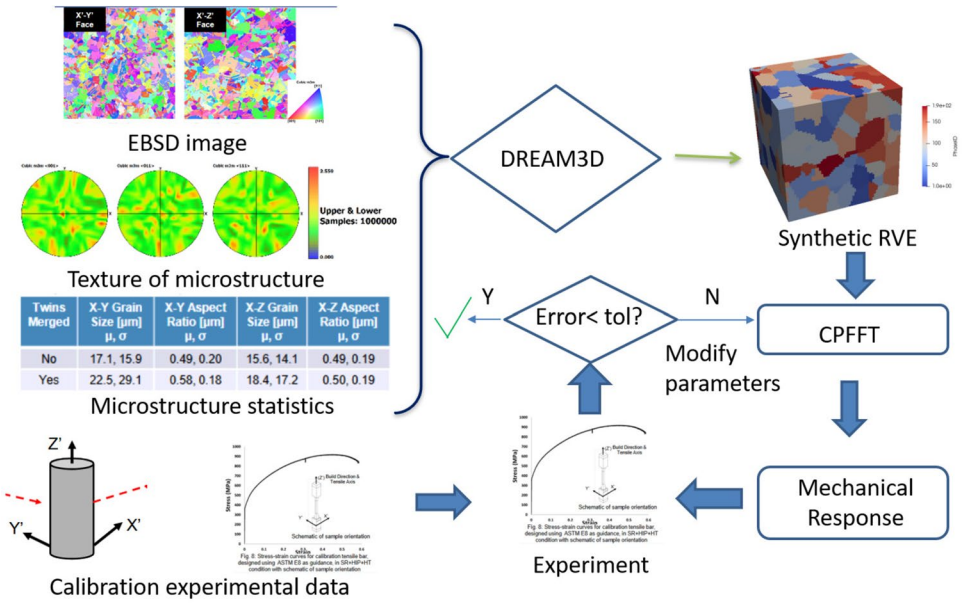

Fig. 3 Schematic diagram showing the steps of the calibration method. CPFFT means crystal plasticity fast Fourier transformation

Calibration Method

Genetic Algorithm

In order to calibrate the crystal plasticity material model, during the challenge the flow-diagram shown in Fig. 3 was followed. The EBSD statistics supplied by the AFRL were used in the open source software package DREAM.3D [40] to create a synthetic representative volume element (RVE). The RVE had dimensions of 10 voxels × 10 voxels × 10 voxels, and each voxel represented 1 grain. Five parameters from the crystal plasticity crystal plasticity formulation given in " Material Modeling Methods" section were calibrated using the genetic algorithm: the deformation resistance shear stress τ_0 (controlling the yield point), direct hardening coefficients (H, h), and dynamic recovery constants (R and r) (controlling the plastic response). By varying these parameters, mechanical response of the RVE was computed and compared with the experimental data provided by the AFRL. The optimization of the parameters was done by the genetic algorithm in MATLAB [12]. When a satisfactory resemblance is achieved, the parameters are considered to be final. Since the genetic algorithm needs a large number of iterations, the five parameters were calibrated sequentially. First τ_0, H, and R were calibrated. In the second stage, h and r were calibrated. The result of the calibration is shown in Fig. 4. For the competition stage, the calibrated parameters from the genetic algorithm were used. Later, in the post-competition stage, a PGD-based calibration method was adopted, which will be explained in the next section "Proper Generalized Decomposition-Based Material Parameter Identification". In both cases, elastic parameters are taken from the supplementary information provided with the AFRL challenge 4 statement, collected from [41]. Final calibration values for each method are given in Table 1.

Proper Generalized Decomposition-Based Material Parameter Identification

We propose using a PGD-based surrogate modeling approach [10, 11] for calibration or material model parameter identification as an enhancement over the previously described genetic algorithm.

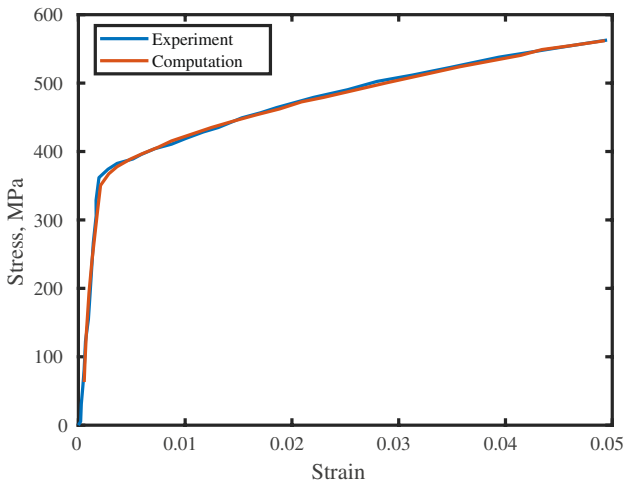

Fig. 4 Calibration outcome for optimization using a genetic algorithm

The PGD method used in our work is the higher-order PGD (HOPGD), which is designed for non-intrusive data learning and constructing reduced order surrogate models.

Journal : Large 40192 | Article No : 208 | Pages : 15 | MS Code : 208 | Dispatch : 4-5-2021

Table 1 Summary of calibrated parameters from calibration cases. All the parameters are specified for convenience of the reproduction of the readers. Only τ_0, H, h, R, and r are calibrated. Other parameters were selected from literature

Material property	Genetic algorithm values	PGD values
C1111*	245587 MPa	245587 MPa
C1122*	158173 MPa	158173 MPa
C2323*	118901 MPa	118901 MPa
$\dot{\gamma}_0$	0.00242	0.00242
m	58.8	58.8
τ_0	131.5 MPa	143.9 MPa
a	1.4	1.4
H	0.0	0.0
h	0.0	0.43
R	2892.93	2500
r	13.02	30

* From [41]

The basic idea behind PGD approaches is separation of variables. For a d-dimensional function $f(\mu_1, \mu_2, ..., \mu_d)$, which contains the quantity of interest as a function of parameters $\mu_i|_{i=1,d} \in \mathcal{D}_i$, the separation of variables results in the following form

$$f(\mu_1, \mu_2, ..., \mu_d) \approx f^n(\mu_1, \mu_2, ..., \mu_d) = \sum_{m=1}^{n} F_1^m(\mu_1) F_2^m(\mu_2) \cdots F_d^m(\mu_d) \tag{12}$$

where f^n is an approximation of f, n is the rank of approximation, m denotes the m^{th} mode. Note that the superscripts n, m are counting indices, not exponentiation. The n-rank approximation f^n is given by the finite sum of products of the separated functions: $F_i^m|_{i=1,d}$, which are a priori unknown and should be obtained either with a pre-computed database [10, 11, 32, 42] or by directly resorting to physical models [29–31, 43]. Furthermore, each function F_i^m that represents a variation of the original function f in the parameter direction μ_i is also called a mode function.

The HOPGD relies on the database and falls into the family of data-driven approaches. The database can be either from simulations or experiments. Once the database is obtained, the HOPGD can learn with data to compute the mode functions $F_i^m|_{i=1,d}$, which can reproduce (or extrapolate) the full parametric function f. Therefore, HOPGD can be used to construct a surrogate model that relates the input parameters and output quantity of interest. The detailed implementation of the method is presented in [10] and summarized in Appendix A. Examples of codes can be found on the GitHub project (https://yelugit.github.io/hopgd/).

In this work, the parametric stress–strain curve is required for materials identification. More specifically, we want a surrogate model relating the parameters and the stress–strain curve. The PGD surrogate model can be written as

$$\sigma^{\text{PGD}} = \sigma^n(\epsilon, p_1, ..., p_d) = \sum_{m=1}^{n} F_\epsilon^m(\epsilon) F_1^m(p_1) \cdots F_d^m(p_d) \tag{13}$$

where p_i are the parameters we want to identify for the crystal plasticity model. Once this surrogate model is obtained, we can easily vary the values of those p_i and find the best set for a given experimental measure, instead of repetitively running the expensive FFT simulation.

Now, assuming the parameters $\boldsymbol{p} = [p_1, \ldots, p_d]$ belong to a predefined domain $\mathcal{D} = \mathcal{D}_1 \times \cdots \times \mathcal{D}_d$, we want to identify the best $\boldsymbol{p}^*$ such that

$$\boldsymbol{p}^* = \arg\min_{\boldsymbol{p} \in \mathcal{D}} J\left(\sigma^{\text{PGD}}, \sigma^e, \boldsymbol{p}\right) \tag{14}$$

where J denotes the objective function which measures the distance between the model output σ^{PGD} and the experimental measurement σ^e. Now, we can repetitively perform the following steps to find the best parameters:

1. Sample the parameter space $\mathcal{D}$ with the adaptive strategy, as described in Appendix B.
2. Compute the stress–strain curve data with the crystal plasticity model for the selected data points.
3. Use HOPGD and data samples to compute the mode functions in Eq. (13) and obtain the surrogate model σ^{PGD}.
4. Use the surrogate model to optimize the parameters to match the experimental data. Solve Eq. (14).

We remark here that the surrogate model used in the above procedure is extremely cheap to evaluate, since the mode functions $F_i^m(p_i)$ are known with data and we only need to perform a 1D interpolation to get the output σ for a given point $\boldsymbol{p}$. The same procedure has been applied to a welding problem and shown to have very good performance in terms of efficiency [11]. In what follows, PGD refers to HOPGD unless otherwise stated.

In the post-competition stage, we explored several ideas to improve our predictions. In one case, we took the calibration data provided by the AFRL and used PGD to calibrate the material model. The results are shown in Fig. 5. The model and experiment appear to agree well. However, based on discussion at the AFRL Workshop follow the competition, we also tried calibrating the material model directly to the experimental data used to assess the competitors and provided as an overall stress–strain curve by AFRL. It seemed more logical as the challenge asked

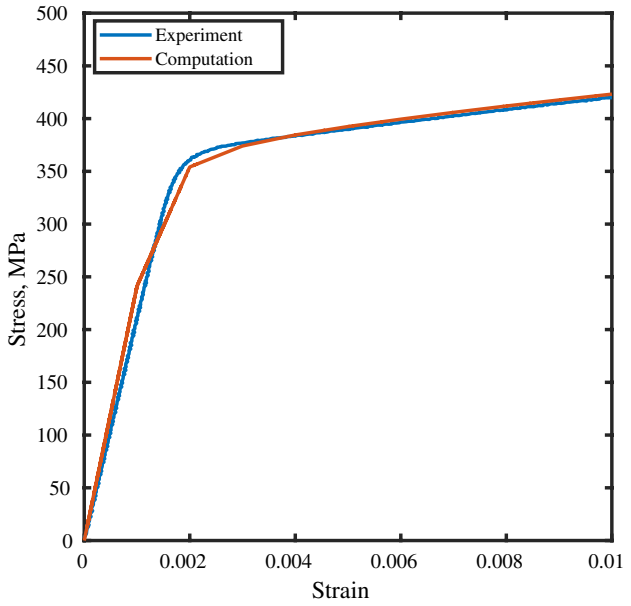

Fig. 5 Calibration outcome for optimization using the PGD method with calibration data from AFRL

to predict the local values based on this exact experiment. The result of this second calibration is shown in Fig. 6. The load drops required for in situ data collection in the challenge specimen were manually removed to enable the calibration. Here again, we see very good comparison between the experiment and simulation. The most significant improvement, thus, is the computational time. For both the genetic algorithm and PGD-based calibration, 36 2.3 GHz Xeon Gold 6140 processors were used with 192 GB of memory. For the genetic algorithm, the calibration took 3.6 h. Compared to that, the first calibration (with calibration data) with PGD took 0.7 h. Final calibration with the PGD algorithm with the final experimental results took around 0.8 h, representing a speed up factor of almost 4.2.

Discussion of Results

Comparison of Absolute Errors Between Elastic and Total Strain

The crystal plasticity method computes total strain (elastic plus plastic), from which elastic strains can be extracted. Here, we will report both elastic and total strain predictions; total strains are different from both the elastic predictions and elastic measurements, indicating the likelihood that plastic components of strain are substantial. Importantly, we must be cognizant of the differences when performing model validation. A comparison of the results between the PGD-calibration method and genetic

Fig. 6 Calibration outcome for optimization using PGD with exact experimental data from the AFRL challenge specimen, with load drops induced by data collection manually removed for calibration

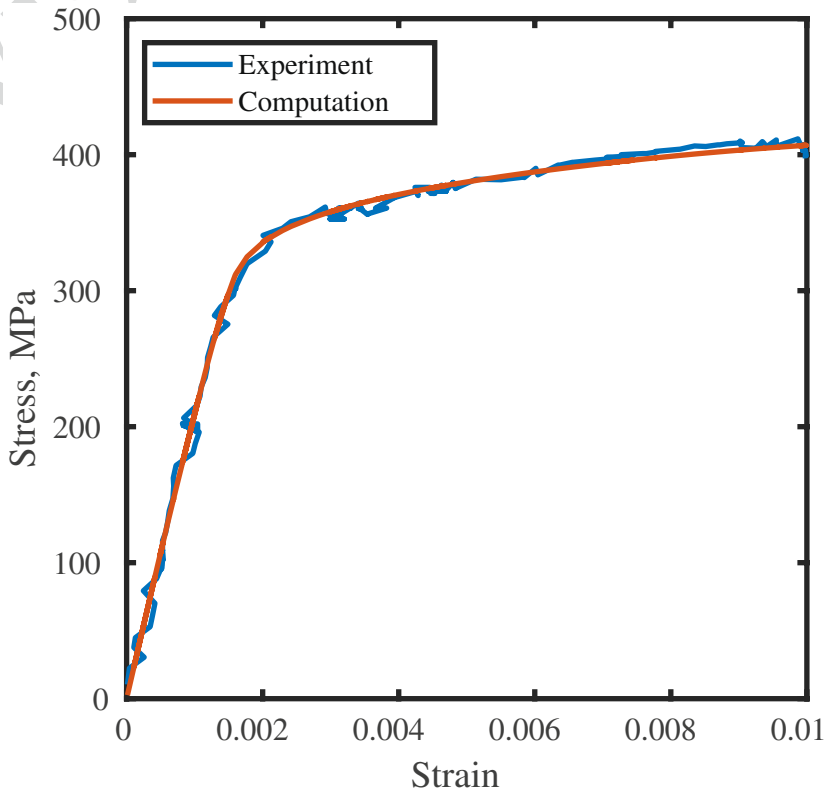

Journal : Large 40192 | Article No : 208 | Pages : 15 | MS Code : 208 | Dispatch : 4-5-2021

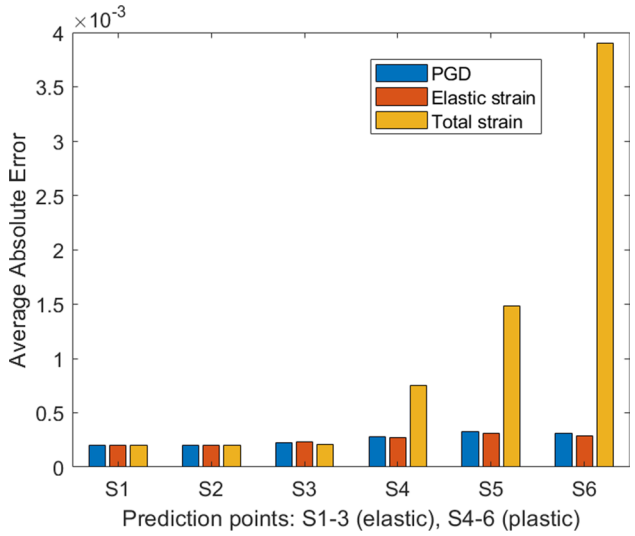

Fig. 7 Average absolute error measured as the absolute error between predicted and measured strain averaged across the 28 challenge grains, in E_{xx} for PGD, elastic, and total strain reported

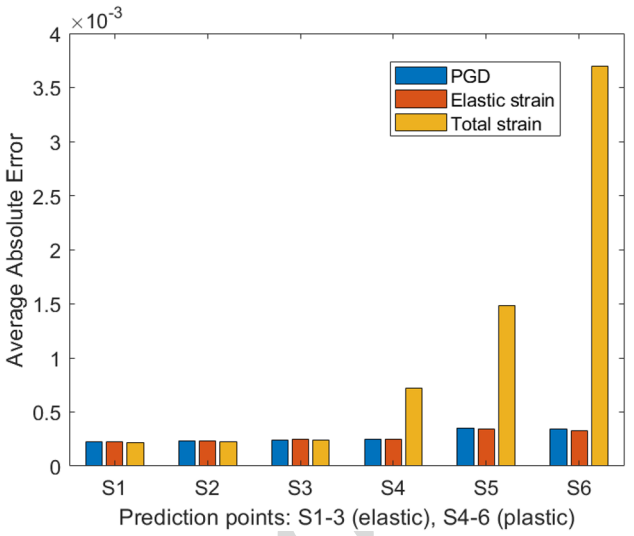

Fig. 9 Comparison of absolute error in E_{zz} for PGD, elastic, and total strain reported

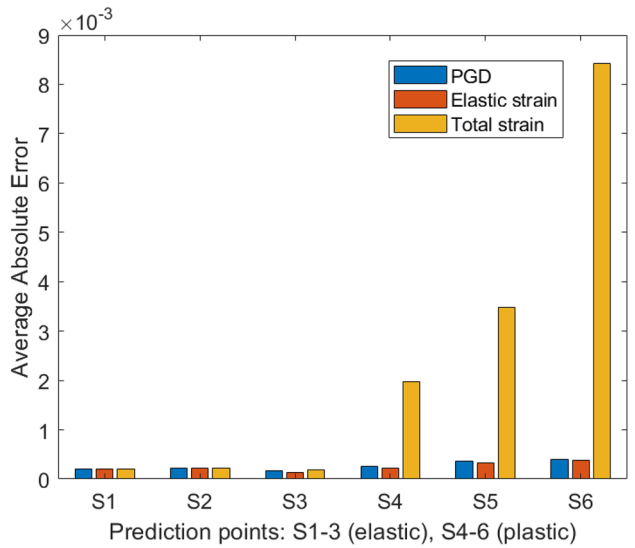

Fig. 8 Comparison of absolute error in E_{yy} for PGD, elastic, and total strain reported

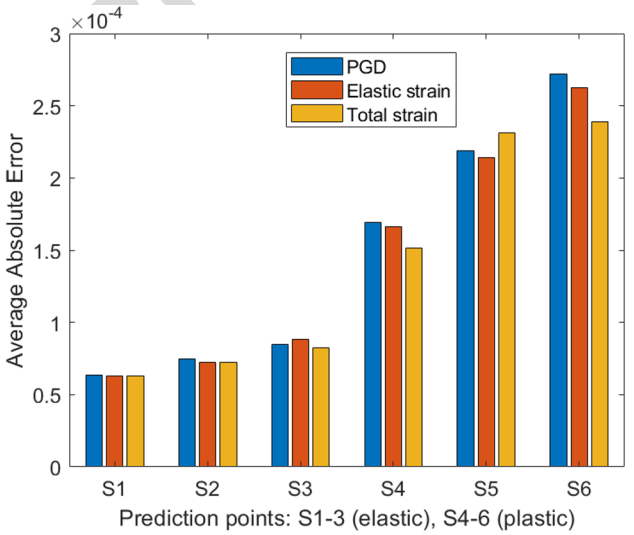

Fig. 10 Comparison of absolute error in E_{xy} for PGD, elastic, and total strain reported

algorithm-based method is presented for elastic strain predictions. Some key takeaways highlighting the capability of the solution method are also mentioned.

A comparison of average absolute error in experimentally measured elastic strains along the normal directions (X, Y, and Z axes) E_{xx}, E_{yy}, E_{zz} for total and elastic strain predictions is shown in Figs. 7, 8 and 9. The absolute error is defined as the absolute value of the difference between the experimental data provided by AFRL and our predicted strain. There were in total 28 challenge grains, so for each prediction point, the average absolute error shown is the absolute error averaged over the 28 grains. When the total strain is reported, the results are far off from the experimental data, especially in the plastic regime of the stress–strain curve. This is expected, because the experimental results only measure the elastic component of the strain in both the elastic and plastic zones. For the elastic zone, both predictions give a more or less similar result. This is expected as the prediction of grain average elastic strain depends on the elastic constant used in the computation. In both total and elastic strain predictions, the elastic constants are the same. Another important observation is

Journal : Large 40192 | Article No : 208 | Pages : 15 | MS Code : 208 | Dispatch : 4-5-2021

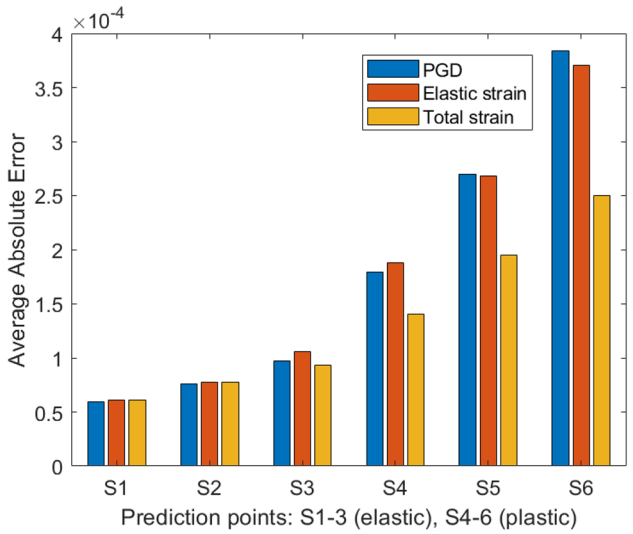

Fig. 11 Comparison of absolute error in E_{yz} for PGD, elastic, and total strain reported

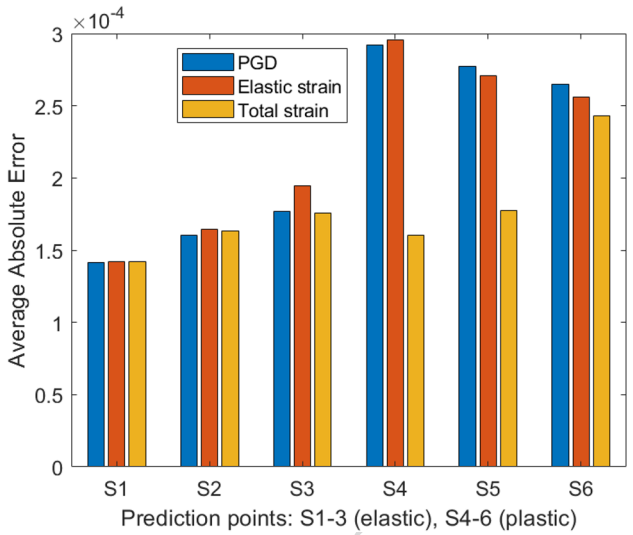

Fig. 12 Comparison of absolute error in E_{xz} for PGD, elastic, and total strain reported

that the prediction performance is better for the E_{yy} component compared to the other two normal directions. This is the loading direction, and strains in this direction are much larger in magnitude than for the other directions. The shear strain predictions are presented in Figs. 10, 11 and 12. Interestingly, the difference of absolute errors between the elastic strain and total strain cases for shear components is much less compared to their normal counterparts. It appears that the shear strain components are closer to experimental value when the total strain was reported. The reasoning would be for shear components of strain, the amount of plastic strain is negligible according to our calculation.

The challenge requested only grain-averaged strain values. However, in this prediction framework, we also predict the local strain distribution inside each grain. Table 2 shows the prediction of grain average strain component of E_{xx} for challenge grain 12602. A demonstration of the local deformation field is presented in Figs. 13 and 14. The method uses the voxel-wise discretization of the domain and treats each voxel as a material point. The solution is given at each such material point. In order to sufficiently resolve the material, many material points within each grain are required. Thus, the method inherently captures both stress and strain locally within each grain. Specifically, for each applied displacement step, boundary conditions in terms of macroscopic deformation gradients are applied homogeneously throughout the domain and an iterative scheme is used to ensure compatibility within the domain, using the two-stage decomposition of plastic deformation common to many crystal plasticity routines. Further details of the method can be found in [37, 44]. In Fig. 13, the distribution of deformation gradient along the *Y*-axis is shown in the reference configuration at (a) S1 and (b) S6. Thus, with this method it is possible to identify sub-grain level deformation due to the applied loading conditions. Such capability is likely important for modeling damage because localized deformation drives damage evolution, such as for fatigue failure. Figure 14 shows the local changes in deformation gradient within challenge grain 12602.

Comparison of PGD-Based Method and Genetic Algorithm

The PGD-based calibration method is applied to calibrate the five parameters simultaneously. The final values of these parameters are compared with the genetic algorithm, as shown in Table 2. In our work, we observed similar final solutions between PGD and genetic algorithm. This is confirmed by Figs. 14 and 5. However, in a general sense,

Table 2 Summary of reported values for strain component E_{xx} in challenge grain 12602 at the six reporting points

Prediction state	S1	S2	S3	S4	S5	S6
Total strain	0.000192	0.000225	0.000269	0.000791	0.001662	0.004119
Elastic strain	0.000192	0.000225	0.000281	0.000411	0.000274	0.000262
PGD calibration	0.000192	0.000225	0.000281	0.000421	0.000314	0.000313

Journal : Large 40192 | Article No : 208 | Pages : 15 | MS Code : 208 | Dispatch : 4-5-2021

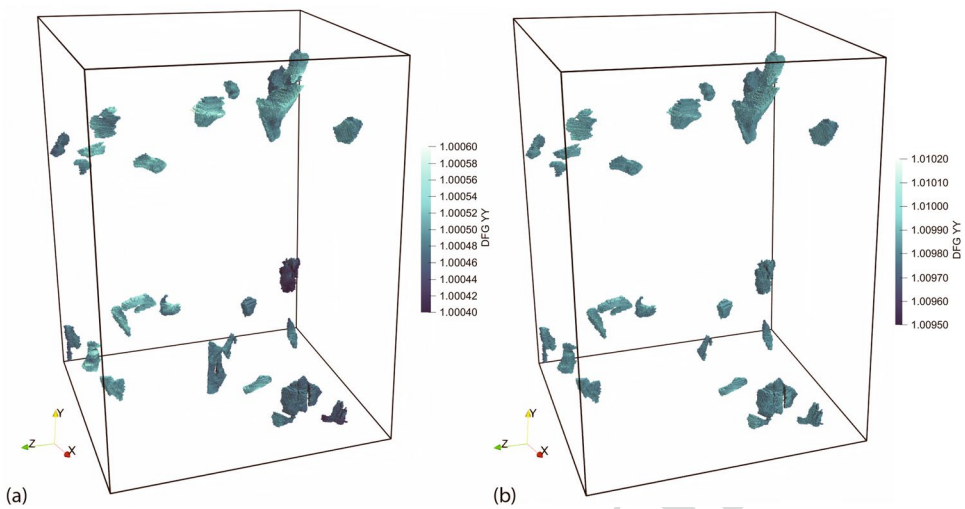

Fig. 13 Representation of the predicted local YY-component of deformation gradient (in the loading direction) for the challenge grains at **a** S1, and **b** S6. Note that the color scale bars are different, because the deformation gradients are substantially larger in S6

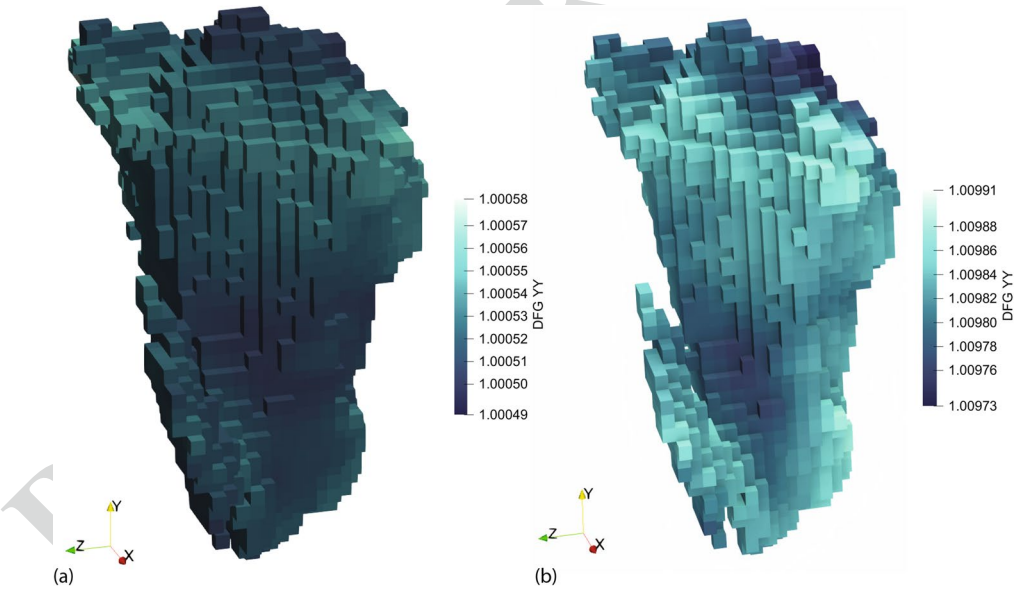

Fig. 14 Distribution of the YY component of the deformation gradient in challenge grain 12602 at **a** strain point 1, and **b** strain point 6. The deformed configuration is shown with a factor of ten increase in the deformation field. Note that the color scales on (**a**) and (**b**) are different, so that the deformations can be seen within the grains more clearly

since the genetic algorithm usually converges to some local minimums, the final solution could be less optimal for the genetic algorithm than the PGD method, i.e., confidence in obtaining a best-case optimization is lower for the genetic algorithm. The genetic algorithm may also be sensitive to the initial settings, e.g., initial guesses, initially prescribed parameter space.

In the post-competition stage, the results were reproduced using new calibration values. The absolute average error compared to the experimental data is shown in Figs. 6, 7, 8, 9, 10, and 11. Just like in the previous section, the presentation of results is divided into elastic and plastic zones for all the grains identified at different experimental points. In all the figures, one can observe that the difference of error between the PGD-calibrated prediction and genetic algorithm is small. Hence, it is confirmed that the PGD-calibrated material model can achieve the same level of accuracy as the genetic algorithm calibrated model, at least in this case. This has significant implications for the computational aspects of calibration for large-scale problems

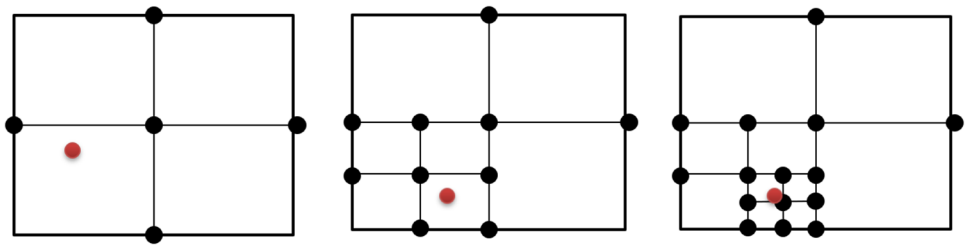

(a) Grid at level 1 (b) Grid at level 2 (c) Grid at level 3

Fig. 15 Adaptive sampling strategy for data generation. Black: sampling pints (data), Red: current optimum

using crystal plasticity. Using this fast and advanced material identification technique, calibration can be more detailed and more demanding material models with broader parameter sets can also be used to solve practical problems.

Conclusions

The PGD-based method of calibration is a promising alternative to the more conventional genetic optimization-based methods for calibration of complex material models. The article shows the evidence of the efficacy of the method by showing the prediction for both genetic optimization method and PGD-based method. The FFT-based method used in this article is a viable alternative to using finite element-based methods, in this case. In addition, although the challenge asked for prediction of local grain-average elastic strain tensor, the method can also predict local strain or stress fields. In future, a combined data-driven material parameter identification method with mechanistic data-driven reduced order methods may be developed, so that both prediction and calibration become faster and thus more useful for design of materials.

Appendix A: Data-Driven PGD-Based Surrogate Modeling

For computational purposes, the PGD approximation [10] can also be written in the following incremental form by considering that the f^{n-1} is computed previously

$$f^n(\mu_1, \mu_2, ..., \mu_d) = f^{n-1} + F_1^n(\mu_1)F_2^n(\mu_2)\cdots F_d^n(\mu_d) \tag{15}$$

or for notation simplification,

$$f^n(\mu_1, \mu_2, ..., \mu_d) = f^{n-1} + F_1(\mu_1)F_2(\mu_2)\cdots F_d(\mu_d) \tag{16}$$

Assuming a database of f is known for some selected sampling points in the parameter space $\mathcal{D} = \mathcal{D}_1 \times \cdots \times \mathcal{D}_d$, the HOPGD seeks an L^2 projection of the data as follows [10]:

$$\begin{cases} \text{Find } f^n \in V_n \subset L^2(\mathcal{D}) \text{ s.t.} \\ f^n = \underset{f^{n*}\in V_n}{\arg\min}\left(\frac{1}{2} \parallel wf^{n*} - wf \parallel^2_{L^2(\mathcal{D})}\right) \end{cases} \tag{17}$$

where w is a sampling index equal to 1 or 0, depending on the sampling strategy in the parameter space $\mathcal{D}$. This means the approximated function f^n minimizes only the error on selected sampling points.

Considering the incremental form of f^n (16), the problem (17) can be converted to a local minimization problem as below.

$$\begin{aligned}(F_1, \dots, F_d) = \underset{F_1^*\in L^2(\mathcal{D}_1),\dots,F_d^*\in L^2(\mathcal{D}_d)}{\arg\min} \frac{1}{2} \parallel wf^{n-1} \\ + w\prod_{i=1}^{d} F_i^* - wf \parallel^2_{L^2(\mathcal{D})}\end{aligned} \tag{18}$$

which can be equivalently written in an integral form with $(F_1, \dots, F_d)$ as unknown variables to solve

$$\begin{aligned}&\int_{\mathcal{D}} w\prod_{i=1}^{d} F_i \delta f \, d\mu_1 \dots d\mu_d \\ &= \int_{\mathcal{D}} (wf - wf^{n-1})\delta f \, d\mu_1 \dots d\mu_d\end{aligned} \tag{19}$$

where the test function $\delta f = \delta \prod_{i=1}^{d} F_i = \delta F_1 F_2 ... F_d + \cdots + F_1 F_2 ... \delta F_d$. Thus, for a target function f and having estimated the $n-1$ rank of PGD approximation f^{n-1}, the next step consists of computing the new separated modes $F_1, F_2, ..., F_d$ at rank n using the above equation.

An alternating fixed point algorithm can be used to solve this problem for the mode functions. The rank n can start from 1 and incrementally increases to a finite number which is determined by the convergence of the approximation, i.e., $\|wf - wf^n\| \leq \varepsilon \|wf\|$. More details can be found in [10]. Sparse sampling can overcome the exponentially increasing complexity of the right-hand side integral in equation (19).

Appendix B: Sampling Strategy for PGD-Based Materials Identification

The sampling strategy adopted in our work was proposed by [11]. We summarize here the main idea of the methodology. Assuming a parameter space $\mathcal{D}$ (usually large enough) has been chosen, we aim at limiting the necessary number of data points in the parameter identification procedure. Hence, the idea consists in incrementally enriching the database and using the optimization results to guide the sampling. This results in an adaptive sparse grid in $\mathcal{D}$ and is suitable even for a high dimensional space. The main procedure is shown as below and in Fig. 15.

- Start from the predefined space $\mathcal{D}$, sample the central axes of the space by adding two points at the extremities of each axis and one point at the center. In a two-dimensional space, this axis sampling results in a sparse grid of five points, as shown in Fig. 15a. Analogically, for an n-dimensional space, this number of points is $2n + 1$, which scales only linearly with n. This is advantageous for high dimensionality cases.
- With the first-level sampling, we can construct the first PGD surrogate model and perform a first round of optimization by following the 4 steps described in the "Proper Generalized Decomposition-Based Material Parameter Identification" section. This optimization can be done with a gradient-based algorithm (e.g., SQP) with a multi-start strategy [11] for finding the global optimum. Here we can simply compare the final objective function J of different local minimums and chose the best one as the global optimum. An example of this is indicated by a red point in Fig. 15a.
- Since the quality of the PGD model is based on data (i.e., grid), we need to further sample the space $\mathcal{D}$ to check the convergence. The idea is to go into a sub-level of the space, where the global optimum is located, then perform the axis sampling in that subspace, see, e.g., Fig. 15b. The global optimum will be changed with the updated PGD model or stay close to the previous one. Depending on whether convergence is reached, the space can be further sampled in the same way or considered as the final one. In Fig. 15, convergence is clearly reached at level 3.

Remark: the optimization at each level has to be done with initial guesses randomly chosen in the global space $\mathcal{D}$, even though the data enrichment is locally performed.

Appendix C: FCC slip systems

See Table 3.

Table 3 Miller indices of active the slip directions and planes for an FCC crystal lattice

Slip system number	slip direction	slip plane	Slip system number	slip direction	slip plane
1	$[\bar{1}01]$	(111)	7	[101]	$(\bar{1}11)$
2	$[\bar{1}10]$	(111)	8	[110]	$(\bar{1}11)$
3	$[0\bar{1}1]$	(111)	9	$[0\bar{1}1]$	$(\bar{1}11)$
4	[011]	$(\bar{1}\bar{1}1)$	10	[011]	$(1\bar{1}1)$
5	$[\bar{1}10]$	$(\bar{1}\bar{1}1)$	11	[110]	$(1\bar{1}1)$
6	[101]	$(\bar{1}\bar{1}1)$	12	$[\bar{1}01]$	$(1\bar{1}1)$

Journal : Large 40192 | Article No : 208 | Pages : 15 | MS Code : 208 | Dispatch : 4-5-2021

Acknowledgements The authors would like to acknowledge the support of National Science Foundation (NSF, USA) grants CMMI-1762035 and CMMI-1934367; and award no. 70NANB19H005 from U.S. Department of Commerce, National Institute of Standards and Technology as part of the Center for Hierarchical Materials Design (CHiMaD), USA. This work was completed while Orion Kafka held a National Research Council Postdoctoral Research Associateship at the National Institute of Standards and Technology.

Declarations

Conflict of interest The authors report no conflicting interests.

References

1. Francois MM, Sun A, King WE, Henson NJ, Tourret D, Bronkhorst CA, Carlson NN, Newman CK, Haut TS, Bakosi J et al (2017) Modeling of additive manufacturing processes for metals: challenges and opportunities. Curr Opin Solid State Mater Sci, 21(LA-UR-16-24513; SAND-2017-6832J)
2. Sames WJ, List FA, Pannala S, Dehoff RR, Babu SS (2016) The metallurgy and processing science of metal additive manufacturing. Int Mater Rev 61(5):315–360
3. Smith J, Xiong W, Yan W, Lin S, Cheng P, Kafka OL, Wagner GJ, Cao J, Liu WK (2016) Linking process, structure, property, and performance for metal-based additive manufacturing: computational approaches with experimental support. Comput Mech 57(4):583–610
4. Yihong K, Tan XP, Wang P, Nai MLS, Loh NH, Liu E, Tor SB (2018) Anisotropy and heterogeneity of microstructure and mechanical properties in metal additive manufacturing: a critical review. Mater Design 139:565–586
5. Li C, Liu ZY, Fang XY, Guo YB (2018) Residual stress in metal additive manufacturing. Procedia Cirp 71:348–353
6. Benzing JT, Liew LA, Hrabe N, DelRio FW (2020) Tracking defects and microstructural heterogeneities in meso-scale tensile specimens excised from additively manufactured parts. Exp Mech 60(2):165–170
7. Kafka OL, Jones KK, Yu C, Cheng P, Liu WK (2021) Image-based multiscale modeling with spatially varying microstructures from experiments: demonstration with additively manufactured metal in fatigue and fracture. J Mech Phys Solids 150: 104350
8. Prithivirajan V, Sangid MD (2018) The role of defects and critical pore size analysis in the fatigue response of additively manufactured IN718 via crystal plasticity. Mater Design 150:139–153
9. Michael G (2017) Additive manufacturing in the context of structural integrity. Int J Fatigue 94:168–177
10. Lu Y, Blal N, Gravouil A (2018) Adaptive sparse grid based HOPGD: toward a nonintrusive strategy for constructing space-time welding computational vademecum. Int J Numer Meth Eng 114(13):1438–1461
11. Lu Y, Blal N, Gravouil A (2019) Datadriven HOPGD based computational vademecum for welding parameter identification. Comput Mech 64(1):47–62
12. Chipperfield A, Fleming P, Pohlheim H, Fonseca C (1994) Genetic algorithm toolbox for use with MATLAB. Citeseer
13. Beaudoin AJ, Obstalecki M, Storer R, Tayon W, Mach J, Kenesei P, Lienert U (2012) Validation of a crystal plasticity model using high energy diffraction microscopy. Modell Simul Mater Sci Eng 20(2):024006
14. Prithivirajan V, Ravi P, Naragani D, Sangid MD (2021) Direct comparison of microstructure-sensitive fatigue crack initiation via crystal plasticity simulations and in situ high-energy x-ray experiments. Mater Design 197:109216
15. Turner TJ, Shade PA, Bernier JV, Li SF, Schuren JC, Peter K, Suter RM, Jonathan A (2017) Crystal plasticity model validation using combined high-energy diffraction microscopy data for a Ti-7Al specimen. Metall Mater Trans A 48(2):627–647
16. Air Force Research Laboratory (AFRL) Additive Manufacturing (AM) Modeling Challenge Series. https://materials-data-facility.github.io/MID3AS-AM-Challenge/. February 2021. Accessed 4 March 2021
17. Haouala S, Lucarini S, LLorca J, Segurado J (2020) Simulation of the hall-petch effect in FCC polycrystals by means of strain gradient crystal plasticity and FFT homogenization. J Mech Phys Solids 134:103755
18. Roters F, Eisenlohr P, Hantcherli L, Tjahjanto DD, Bieler TR, Raabe D (2010) Overview of constitutive laws, kinematics, homogenization and multiscale methods in crystal plasticity finite-element modeling: theory, experiments, applications. Acta Mater 58(4):1152–1211
19. Cheng Yu, Kafka OL, Liu WK (2019) Self-consistent clustering analysis for multiscale modeling at finite strains. Comput Methods Appl Mech Eng 349:339–359
20. Lebensohn RA (2001) N-site modeling of a 3D viscoplastic polycrystal using fast Fourier transform. Acta Mater 49(14):2723–2737
21. Kapoor K, Ravi P, Noraas R, Park J-S, Venkatesh V, Sangid MD (2021) Modeling Ti-6Al-4V using crystal plasticity, calibrated with multi-scale experiments, to understand the effect of the orientation and morphology of the α and β phases on time dependent cyclic loading. J Mech Phys Solids 146:104192
22. Rovinellia A, Proudhon H, Lebensohn RA, Sangid MD (2020) Assessing the reliability of fast Fourier transform-based crystal plasticity simulations of a polycrystalline material near a crack tip. Int J Solids Struct 184:153–166
23. Kafka OL, Yu C, Shakoor M, Liu Z, Wagner GJ, Liu WK (2018) Data-driven mechanistic modeling of influence of microstructure on high-cycle fatigue life of nickel titanium. JOM 70(7):1154–1158
24. Liu Z, Kafka OL, Yu C, Liu WK (2018) Data-driven self-consistent clustering analysis of heterogeneous materials with crystal plasticity. In: Advances in computational plasticity, pp 221–242. Springer
25. Deka D, Joseph DS, Ghosh S, Mills MJ (2006) Crystal plasticity modeling of deformation and creep in polycrystalline Ti-6242. Metall Mater Trans A 37(5):1371–1388
26. Bhattacharyya M, Fau A, Nackenhorst U, Néron D, Ladevèze P (2018) A multi-temporal scale model reduction approach for the computation of fatigue damage. Comput Methods Appl Mech Eng 340:630–656
27. Goury O, Amsallem D, Bordas SPA, Liu WK, Kerfriden P (2016) Automatised selection of load paths to construct reduced-order models in computational damage micromechanics: from dissipation-driven random selection to Bayesian optimization. Comput Mech 58(2):213–234
28. Lu Y, Jones KK, Zhengtao G, Liu WK (2020) Adaptive hyper reduction for additive manufacturing thermal fluid analysis. Comput Methods Appl Mech Eng 372:113312
29. Néron D, Ladevèze P (2010) Proper generalized decomposition for multiscale and multiphysics problems. Arch Comput Methods Eng 17(4):351–372
30. Ammar A, Mokdad B, Chinesta F, Keunings R. (2006) A new family of solvers for some classes of multidimensional partial differential equations encountered in kinetic theory modeling of complex fluids. J Nonnewton Fluid Mech 139(3):153–176
31. Modesto D, Zlotnik S, Huerta A (2015) Proper generalized decomposition for parameterized helmholtz problems in heterogeneous

and unbounded domains: application to harbor agitation. Comput Methods Appl Mech Eng 295:127–149
32. Lu Y, Blal N, Gravouil A (2018) Multi-parametric space-time computational vademecum for parametric studies: application to real time welding simulations. Finite Elem Anal Des 139:62–72
33. Tezzele M, Demo N, Stabile G, Mola A, Rozza G (2020) Enhancing CFD predictions in shape design problems by model and parameter space reduction. Adv Model Simul Eng Sci 7(1):1–19
34. Shade PA, Blank Ba, Schuren JC, Turner TJ, Kenesei P, Goetze K, Suter RM, Bernier JV, Li SF, Lind J, Lienert U, Almer J (2015) A rotational and axial motion system load frame insert for in situ high energy x-ray studies. Rev Sci Instrum 86(9):093902
35. Uchic M, Groeber M, Shah M, Callahan P, Shiveley A,Scott M, Chapman M, Spowart J (2016) An automated multi-modal serial sectioning system for characterization of grain-scale microstructures in engineering materials. In: De Graef M, Poulsen HF, Lewis A, Simmons J, Spanos G (eds) Proceedings of the 1st international conference on 3D materials science, pp 195–202. Springer
36. ASTM E8 / E8M-16ae1 (2021) Standard test methods for tension testing of metallic materials
37. Moulinec H, Suquet P (1998) A numerical method for computing the overall response of nonlinear composites with complex microstructure. Comput Methods Appl Mech Eng 157(1–2):69–94
38. Matthias K, Thomas B, Matti S (2014) Efficient fixed point and Newton-Krylov solvers for FFT-based homogenization of elasticity at large deformations. Comput Mech 54(6):1497–1514
39. Frigo M, Johnson SG (2005) The design and implementation of FFTW3. In proceedings of the IEEE, pp 216–231
40. Groeber MA, Jackson MA (2014) Dream 3D: a digital representation environment for the analysis of microstructure in 3D. Integr Mater Manuf Innov 3(1):56–72
41. Wang Z, Stoica AD, Ma D, Beese AM (2016) Diffraction and single-crystal elastic constants of Inconel 625 at room and elevated temperatures determined by neutron diffraction. Mater Sci Eng A 674:406–412
42. Blal N, Gravouil A (2019) Non-intrusive data learning based computational homogenization of materials with uncertainties. Comput Mech 64(3):807–828
43. Ghnatios C, Masson F, Huerta A, Leygue A, Cueto E, Chinesta F (2012) Proper generalized decomposition based dynamic data-driven control of thermal processes. Comput Methods Appl Mech Eng 213:29–41
44. Shakoor M, Kafka OL, Yu C, Liu WK (2019) Data science for finite strain mechanical science of ductile materials. Comput Mech 64(1):33–45